Pergamon

Geochimica et Cosmochimica Acta, Vol. 68, No. 21, pp. 4287–4299, 2004

0016-7037/04 $30.00 + .00

doi:10.1016/j.gca.2004.02.015

Soft X-ray spectroscopic studies of the reaction of fractured pyrite surfaces with Cr(VI)-containing aqueous solutions

COLIN S. DOYLE,[1,*] TOM KENDELEWICZ,[1] BENJAMIN C. BOSTICK,[1,2] and GORDON E. BROWN, JR.[1,3]

[1]Surface and Aqueous Geochemistry Group, Department of Geological & Environmental Sciences, Stanford University, Stanford, California 94305-2115, USA
[2]Department of Earth Sciences, Dartmouth College, Hanover, New Hampshire 03755, USA
[3]Stanford Synchrotron Radiation Laboratory, SLAC, 2575 Sand Hill Road, Menlo Park, California 94025, USA

(*Received August* 28, 2003; *accepted in revised form February* 23, 2004)

Abstract—We have used synchrotron-based soft X-ray core-level photoemission and adsorption spectroscopies to study the reaction of aqueous sodium chromate solutions with freshly fractured pyrite surfaces. Pyrite surfaces were reacted with 50 μM sodium chromate solution at pH 7 for reaction times between 1 min and 37 hr. Additional experiments were performed at pH 2 and pH 4 with 50 μM sodium chromate solutions and at pH 7 with 5 mM solutions. At chromate concentrations of 50 μM, all chromium present on the pyrite surface was in the form of Cr(III), while at 5 mM, both Cr(III) and Cr(VI) were present at the pyrite surface. Minor quantities of oxidized sulfur species (sulfate, sulfite, and zero-valent sulfur) were identified as reaction products on the pyrite surface. The amount of oxidized sulfur species observed on the surface was greater when pyrite was reacted with 5 mM Cr(VI) solutions because the rate of chromium deposition exceeded the rate of dissolution of pyrite oxidation products, effectively trapping Cr(VI) and oxidized sulfur species in an overlayer of iron(III)-containing Cr(III)-hydroxide. This work shows that pyrite, an extremely cheap and readily available waste material, may be suitable for the removal of hexavalent chromium from acidic to circumneutral waste streams. The reduced chromium ultimately forms a coating on the pyrite surface, which passivates the pyrite surface towards further oxidation.

1. INTRODUCTION

Pyrite is the most common sulfide mineral of the Earth's crust and is commonly present in economically important base-metal sulfide deposits. Extraction of the important ore minerals leaves pyrite concentrated in waste piles, where it becomes a source of acid mine drainage, which is a major and widespread environmental problem (Nordstrom and Alpers, 1999; Simón et al., 1999; Nordstrom et al., 2000). Such drainage acidifies surface waters and releases potentially toxic metals to solution. While many studies have chronicled the effect of pyrite oxidation, a microscopic understanding of the oxidation process is needed to help mitigate the resulting problems (see reviews by: Lowson, 1982; Evangelou and Zhang, 1995; Bonnissel-Gissinger et al., 1998; Nordstrom and Alpers, 1999). Synchrotron-based surface science methods are useful for mechanistic investigations of pyrite oxidation because of the ability to vary the incident photon energy, which results in various degrees of surface sensitivity in photoemission measurements (Bronold et al., 1994; Nesbitt et al., 2000), or to use surface-sensitive detection methods such as Auger electron yield in X-ray absorption measurements. Surface-sensitive photoemission and X-ray absorption spectroscopies are useful for identifying the surface species present on pyrite surfaces at the initial stages of oxidation (Pettenkofer et al., 1991; Bronold et al., 1994; Schaufuβ et al., 1998a; Nesbitt et al., 2000). In this work we have reacted pyrite surfaces with aqueous solutions containing chromate, an important environmental contaminant. The study has two complementary goals: (1) to investigate the oxidation of pyrite surfaces and identify reaction intermediates, and (2) to assess pyrite as a potential material for the reductive removal and immobilization of hexavalent chromium from aqueous solution.

Chromium exists in solution in two principal valence states, trivalent Cr(III) and hexavalent Cr(VI). Hexavalent chromium is soluble and considered an environmental problem due to its high toxicity, while trivalent chromium is much less toxic and relatively insoluble. Reaction with pyrite is capable of reducing Cr(VI) to Cr(III), thereby converting carcinogenic chromate into the more benign trivalent form. Such waste treatment strategies are particularly attractive for circumneutral to low pH, high Cr(VI) systems, where acidity produced by the oxidation of pyrite would lower the pH. Electrokinetic studies (Fornasiero et al., 1992; Bebie et al., 1998) on pristine pyrite surfaces have found that the isoelectric point (roughly the pH of zero net charge) lies in the pH range 1.2 to 1.4. At solution pH below the isoelectric point, the surface will possess a net positive charge, and above the isoelectric point the net surface charge will be negative. This indicates that the negatively charged pyrite surface should repel negative anions such as chromate and dichromate. When pyrite surfaces are initially exposed to air or aqueous solution, the pyrite surface becomes coated with oxide-like products such as iron (oxy)hydroxides, with minor amounts of sulfate (Eggleston et al., 1996; Schaufuβ et al., 1998a). Oxide materials have isoelectric points closer to circumneutral pH (Parks, 1965), and the measured isoelectric points of oxidizing pyrite surfaces (Fornasiero et al., 1992; Zouboulis et al., 1995) are due to the coating formed at the mineral-water interface. Such coating formation results in surfaces that are positively charged under acidic to circumneutral pH conditions, and thus, attractive towards chromate or

* Author to whom correspondence should be addressed (cdoyle@pangea.stanford.edu).

dichromate. Macroscopic studies of the removal of Cr(VI) using pyrite (Zouboulis et al., 1995; Benincasa et al., 2002) and pyrite-rich hydrothermally altered andesite (Kim et al., 2002) suggest that Cr(VI) reduction by pyrite is less rapid than by magnetite or ilmenite (White and Peterson, 1996), but nevertheless, effective. The pyrite oxidation rate by dichromate was found to be a noninteger function of surface area, solution pH, and initial dichromate concentration (Chirita, 2003). Another sulfide mineral, the poorly crystalline iron sulfide mackinawite, FeS_{1-x}, removed Cr(VI) from solution at circumneutral pH and over a range of Cr(VI) concentrations (Patterson et al., 1997; Boursiquot et al., 2002).

The oxidation of pyrite under aqueous acidic conditions is generally described by:

$$2FeS_2 + 7O_2 + 2H_2O \rightarrow 2Fe^{2+} + 4SO_4^{2-} + 4H^+ \quad (1)$$

and

$$4Fe^{2+} + O_2 + 4H^+ \rightarrow 4Fe^{3+} + 2H_2O \quad (2)$$

where iron(III) hydroxide may precipitate under some pH conditions:

$$4FeS_2 + 15O_2 + 14H_2O \rightarrow 4Fe(OH)_3 + 8SO_4^{2-} + 16H^+ \quad (3)$$

In both acidic and basic cases, these reactions imply that oxygen is the ultimate electron sink; however as only one, or perhaps two, electrons can be transferred at any one time (Rimstidt and Vaughan, 2003), the actual mechanism is much more complex than the simple mass balance equations shown here. Iron(III) reacts much more readily with the pyrite surface than does molecular oxygen. Consequently, under conditions in which Fe(III) is regenerated by oxidation of Fe(II) by molecular oxygen, as represented by reaction (2), iron(III) may be the most effective oxidant, and the oxidation of pyrite would be described by reaction (4) (McKibben and Barnes, 1986).

$$FeS_2 + 14Fe^{3+} + 8H_2O \rightarrow 15Fe^{2+} + 2SO_4^{2-} + 16H^+ \quad (4)$$

Under neutral and higher pH conditions, the solubility of Fe(III) is low (Fe^{3+} is hydrolyzed to iron(III) oxides). Under these conditions, the concentration of reactive Fe(III) is very low, and the direct oxidation of pyrite by molecular oxygen may dominate pyrite oxidation (Singer and Stumm, 1970; Lowson, 1982; Moses et al., 1987; Evangelou and Zhang, 1995; Nordstrom and Alpers, 1999).

2. MATERIAL AND METHODS

Freshly fractured pyrite single crystals were employed to ensure pristine, unreacted surfaces. A large cubic single crystal of pyrite from the Logroño region of Spain was cut into 5mm by 5mm rods such that all faces were {001}. The rods were then fractured over a solution-containing reaction vessel, providing a fresh (001) surface for each reaction. Chromate solutions were prepared from a 50 mM Na_2CrO_4 stock solution, and pH was adjusted using 0.1M HCl. Samples were prepared by reacting freshly cleaved surfaces with Cr(VI) solutions at various Cr concentrations and pH, for a specified time. Reactions with 50 μM Cr(VI) solutions were performed for 5 min at pHs of 2, 4, and 7. Studies at pH 7 using 50 μM Cr(VI) were also performed for times ranging between 1 min and 37 h. Other pyrite samples were also reacted with 5 mM Cr(VI) for 30 s. Immediately following dosing, samples were mounted on molybdenum sample holders and introduced into our ultra high vacuum (UHV) system via load-lock where 1×10^{-4} Torr pressure was achieved within 2 to 3 min, and were transferred to the UHV analysis chamber within 20 min. X-ray photoemission and X-ray Absorption Near Edge Structure (XANES) spectroscopies were performed on beamline 10–1 at the Stanford Synchrotron Radiation Laboratory, (SSRL). This beamline is a 30-pole wiggler sidestation with a spherical grating monochromator. Our experimental setup has been described previously (Liu et al., 1998; Kendelewicz et al., 1999), so only a brief description will be presented here. Our system consists of interconnected transfer, preparation, and analysis chambers with a base pressure in the analysis chamber of 5×10^{-10} Torr. XPS and XANES spectra were collected with a double pass cylindrical mirror analyzer (CMA). Survey XPS scans were collected at 200 eV pass energy. Iron 2*p* and chromium 2*p* spectra were collected at 100 eV, and S 2*p* were collected at 15 eV. XANES spectra were collected at the oxygen *K*-edge, the chromium L_{II} and L_{III} edges, and the Fe L_{II} and L_{III} edges with simultaneous detection of Auger electron yield (AEY) with the CMA and total electron yield (TEY) via drain current. Since energy calibration was changing during the adjustment of mirrors for maximizing photon flux, photon energy calibration was adjusted during analysis using the signals arising from the chromium and oxygen contained in the beamline optical components. This provided consistent chromium and oxygen 'dips' in the measured I_0 signal.

3. RESULTS AND DISCUSSION

3.1. Composition of the Reacted Surface

The elemental composition of the pyrite surfaces was determined by survey XPS scans on both reacted and unreacted (control) surfaces. Survey scans were collected using 900 eV incident X-rays. Figure 1 presents photoemission data for the air-fractured pyrite surface and surfaces reacted with 50 μM chromate solution at pH 7 for various times. UHV-fractured surfaces showed only Fe and S photoemission, with adventitious contaminants below detection limits (~5% monolayer coverage). Air-fractured surfaces had small quantities of oxygen and adventitious carbon in addition to iron and sulfur, while chromium-dosed samples exhibited chromium, oxygen, and adventitious carbon in addition to iron and sulfur. The amount of iron and sulfur in the near-surface region probed in these experiments decreased with increasing reaction time with 50 μM chromate solution, while there was an increase in chromium and oxygen concentration. Although semiquantitative (Kendelewicz et al., 2000), the data of Figure 2 demonstrate changes to the atomic fractions of iron, sulfur, chromium, and oxygen present in the near surface as the reaction proceeds. Data for UHV-cleaved and air-cleaved surfaces are included to show the extent of reaction with air following cleavage before dosing. The use of empirical atomic sensitivity factors derived for conventional XPS systems is not strictly correct in this case with our increased surface sensitivity; however, the data for the UHV-cleaved surface show that the results give a reasonable agreement with the expected 2:1 ratio of sulfur to iron. The increased surface sensitivity towards iron at the 900 eV incident energy of the measurement results in the slight underestimation of iron present in the calculated atomic fractions.

As time in contact with a 50 μM chromate solution increases, there is an increase in the fraction of chromium and oxygen in the near-surface layer, and an antipathetic decrease in the fraction of both iron and sulfur. The decrease in iron and sulfur concentrations at the surface arises from a combination of two factors: (i) the pyrite surface is covered progressively by

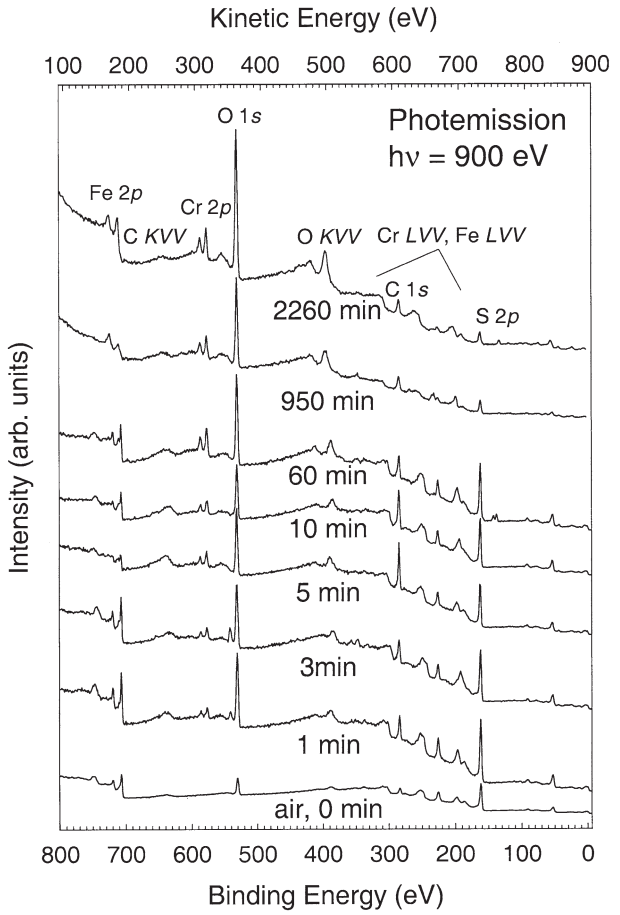

Fig. 1. Survey PES scans showing the Fe 2*p*, S 2*p*, Cr 2*p*, and O 1*s* core levels for freshly fractured pyrite surfaces reacted with 50 μM Cr(VI) solutions at pH 7. Data are shown for reaction times between 1 and 2260 min, along with a zero-time blank, which was air exposed for a time comparable to that for the Cr-exposed samples.

a chromium- and oxygen-containing overlayer, and (ii) oxidized iron and sulfur are removed to solution.

3.2. Reaction Products at the Pyrite Surface

3.2.1. Chromium L-edge X-ray absorption data

Cr *L*-edge XANES spectra were used to determine the oxidation state and coordination environment of chromium on reacted pyrite surfaces. Crocoite ($PbCrO_4$) and chromite ($FeCr_2O_4$) here provide models for tetrahedrally coordinated Cr(VI) and octahedrally coordinated Cr(III). Figure 3 shows Cr L_{II},L_{III}-edge XANES spectra for a series of doses with 50 μM Cr(VI) that range in pH from 2, where dichromate is the dominant, dissolved Cr(VI) species, to 7 where chromate predominates (Cotton and Wilkinson, 1988); data at pH 7 are also presented for 5 mM Cr(VI). All pyrite surfaces reacted with 50 μM Cr(VI) solutions show a signal which is in excellent agreement with the spectrum of chromite, indicting that chromium has been reduced by pyrite to Cr(III). Reaction times at pH 7 of up to 37 h (not plotted) show only a single, Cr(III) signal. Only the pyrite sample reacted with 5 mM Cr(VI) shows both Cr(III) and Cr(VI) on the surface. For this sample using the model compound signals to fit the chromium XANES spectrum, there is ~43% Cr(III), and 57% Cr(VI). The *L*-edge XANES spectra of first row transition elements are strongly dependent on local ligand symmetry and *d*-state occupancy, and thus are quite characteristic of a particular oxidation state and coordination shell (Brydson et al., 1993; de Groot, 1994). The agreement between the XANES of the Cr(III) present on the pyrite surfaces and of the chromite model compound confirms that the Cr(III) present on the pyrite surface is in octahedral oxygen coordination, similar to Cr(III) in Cr(III)-oxide, hydroxide, or oxyhydroxide. Mixed iron-chromium hydroxide coatings were observed on mackinawite (FeS_{1-x}) surfaces when reacted with Cr(VI) solutions (Patterson et al., 1997), according to:

$$3CrO_4^{2-} + 2FeS + 9H_2O \rightarrow 4[Cr_{0.75},Fe_{0.25}](OH)_3 + Fe^{2+} + S_2O_3^{2-} + 6OH^- \quad (5)$$

The same sort of reaction may occur on pyrite surfaces, with disulfide as a reactant. Previous investigations of chromate reacting at magnetite (Fe_3O_4) and surface-oxygen deficient (reduced) hematite (α-Fe_2O_3) surfaces (Kendelewicz et al., 1999; Kendelewicz et al., 2000) have shown that Cr(VI) reduction proceeds until a mixed iron(III)-chromium(III) (oxy)hydroxide layer approximately 15 to 20 Å thick is produced. At that point, electron transfer from Fe(II) centers no longer occurs, reduction rate decreases, and chromate is sorbed at the chromium (III) (oxy)hydroxide surface. The presence of both

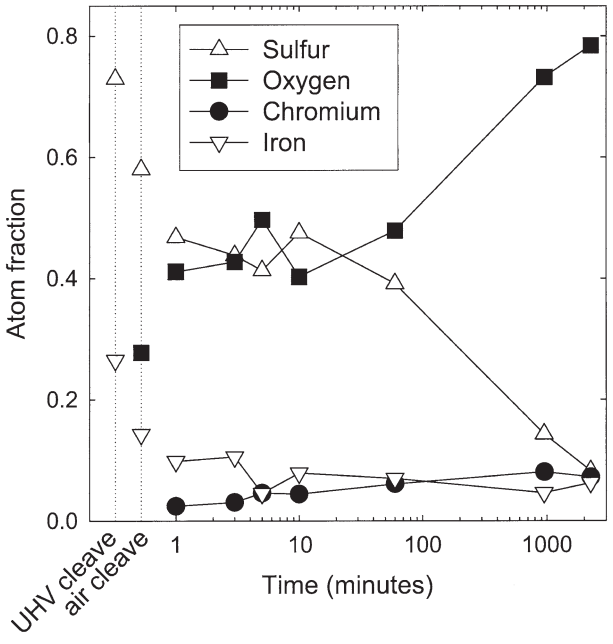

Fig. 2. Calculated atomic fractions of iron, sulfur, chromium, and oxygen in the near-surface region of pyrite surface reacted with 50 μM Cr(VI) at pH 7 as a function of reaction time. The fractions were calculated from fits to the Fe 2*p*, S 2*p*, Cr 2*p*, and O 1*s* core levels. A zero-time blank was also measured, which was exposed to air for a time comparable to air exposure involved in the dosing. The data for the zero-time blank, labeled 'air cleaved' along with data from a UHV cleaved surface is plotted to the left of the dosing data.

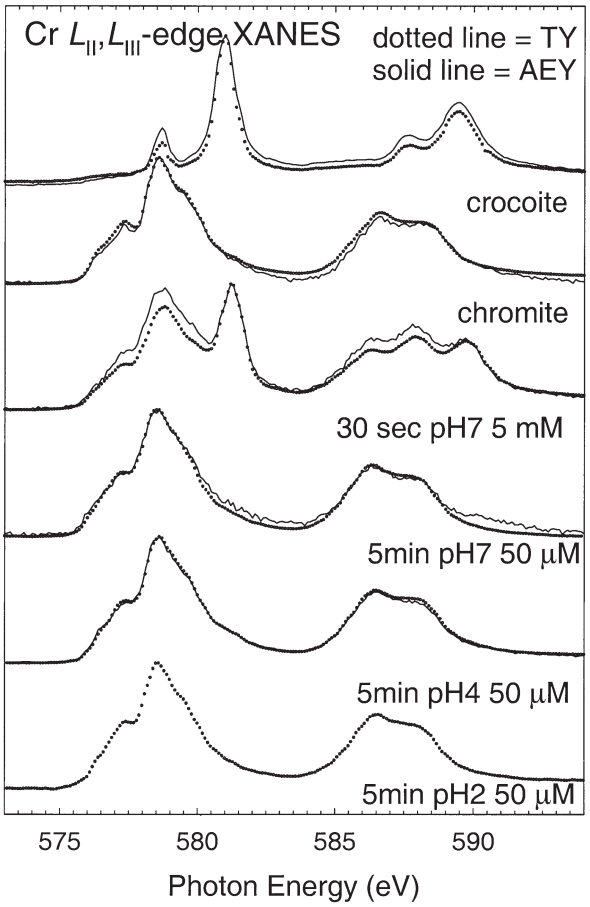

Fig. 3. Chromium L_{II},L_{III}-edge XANES showing the speciation of chromium at the pyrite surface after 5 min reacting with 50 μM Cr(VI) solution at pH 2, pH 4, and pH 7, and 30 s with 5 mM Cr(VI) at pH 7. The minerals crocoite ($PbCrO_4$) and chromite ($FeCr_2O_4$) are included as model spectra for tetrahedral Cr(VI) and octahedral Cr(III) respectively. Solid lines indicate Auger electron yield data, and broken lines are total electron yield data.

Cr(III) and Cr(VI) on the pyrite surface following dosing with 5 mM Cr(VI) is consistent with such a mechanism.

3.2.2. S 2p photoemission data

There is a large body of photoemission work (e.g., Pettenkofer et al., 1991; Peisert et al., 1994; Laajalehto et al., 1997; Guevremont et al., 1998a; Guevremont et al., 1998b; Nesbitt et al., 1998; Schaufuß et al., 1998a; Schaufuß et al., 1998b; Descostes et al., 2000; Nesbitt et al., 2000; Uhlig et al., 2001) directed at understanding the surface species present on the pyrite surface following oxidation. There are a number of competing theories as to the reactive intermediates (Goldhaber, 1983; Sasaki et al., 1995; Luther, 1997; Sasaki et al., 1997) and the possible mechanisms of pyrite oxidation (Singer and Stumm, 1970; Luther, 1987; Moses et al., 1987; Nesbitt and Muir, 1994; Eggleston et al., 1996; Rosso et al., 1999a; Rosso et al., 1999b).

S2*p* photoemission spectra for a pristine, unreacted pyrite surface and Cr(VI)-reacted surfaces and examples of chromium-free aqueous treatments under the same pH conditions are shown in Figure 4. The spectrum of fractured pyrite is typical of the surfaces prepared by this method, showing bulk and surface-shifted disulfide signals (162.4 and 161.8 eV, respectively) and a minor signal at lower binding energy due to monosulfide (S^{2-}) defects at the surface, produced when the S—S bond of the disulfide group ruptures during cleavage (Nesbitt et al., 1998; Nesbitt et al., 2000). While this feature is present on UVH-fractured surfaces, it is rapidly converted to sulfate when exposed to air (Schaufuß et al., 1998a; Schaufuß et al., 1998b), or is lost from the surface altogether when exposed to aqueous solution, as shown here. For doses performed between pH 2 and 7 with 50 μM Cr(VI), there is a slight decrease in the intensity of the surface-shifted disulfide peak relative to the bulk disulfide peak, as was noted for air-exposed pyrites by Schaufuß (1998a; 1998b), consistent with the increased reactivity of the undercoordinated surface sulfur of the disulfide group, which gives rise to the surface-shifted signal. A weak signal, and increased background, in the 166 to 170 eV range indicate oxidized sulfur species, which can be fit with a mixture of sulfur species with binding energies corresponding to sulfur oxidation states ranging from 0 to +6 (S^0 through to SO_4) (Schaufuß et al., 1998a). The surface of

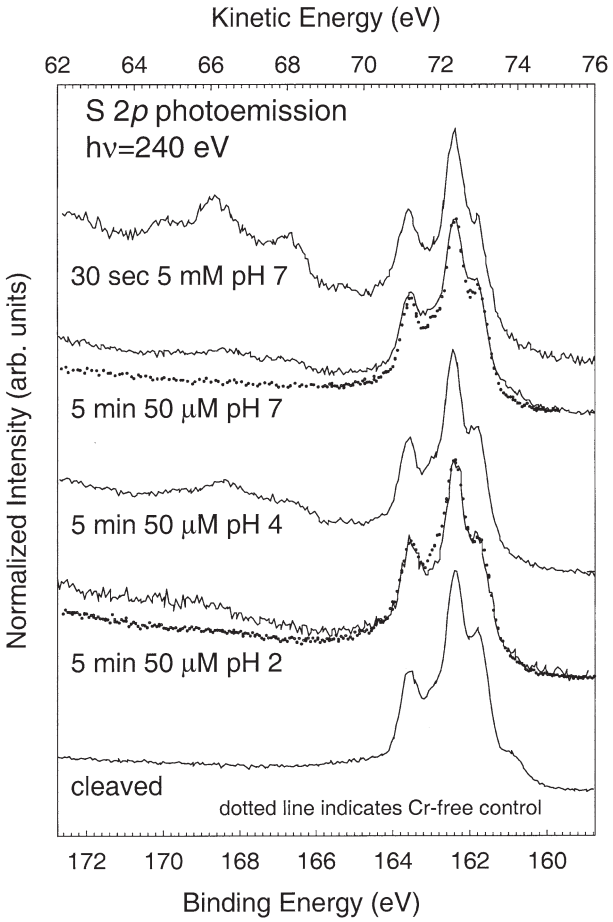

Fig. 4. Surface sensitive S 2*p* photoemission from pyrite surfaces following 5 min reaction with 50 μM Cr(VI) solution at pH 2, pH 4, and pH 7, and 30 s with 5 mM Cr(VI) at pH 7. Spectra for Cr-free solutions under similar pH conditions are included as broken lines, and the spectrum of a UHV-fractured surface is also shown for comparison.

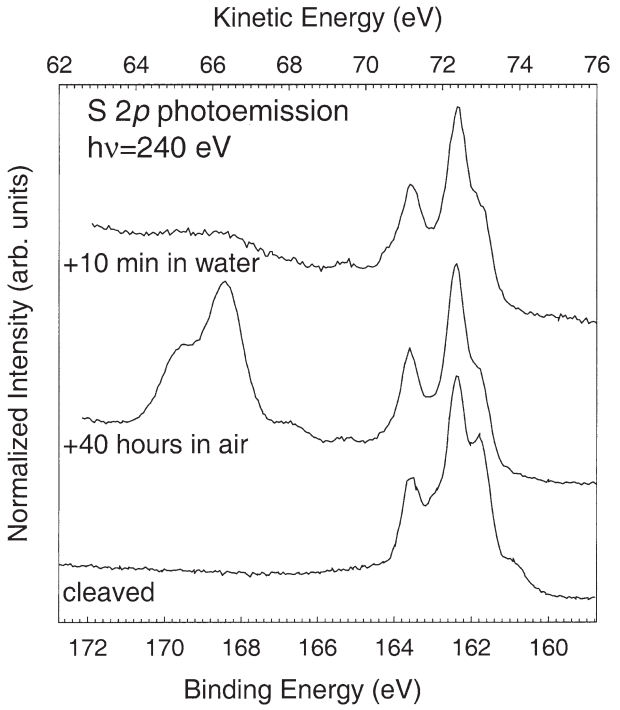

Fig. 5. Surface sensitive S 2*p* photoemission from pyrite surfaces illustrating the loss of sulfate from the surface into solution through a series of sequential treatments applied to a single sample. The lower spectrum is from a UHV-fractured pyrite surface. The middle spectrum is from fractured surface following air exposure for 40 h. The upper spectrum is from this surface dunked in water for 10 min.

pyrite did not show significant differences in S 2*p* photoemission throughout the extended dosing scheme at pH 7; consequently the data shown in Figure 4 for the 5 min reaction are typical of the sulfur surface species observed, with an increased high-binding energy background and weak signals in the binding energy region where sulfate, sulfite, and thiosulfate peaks occur. When dosed with 5 mM Cr(VI), there is clear evidence of oxidized sulfur species, predominantly sulfate and sulfite, on the pyrite surface. We hypothesize that these species would be lost into solution if not for the rapidly deposited chromium oxyhydroxide coating trapping these soluble reaction products.

The loss of sulfate and other soluble reaction products from the surface is illustrated by data in Figure 5, which presents a series of S 2*p* photoemission spectra from a fractured pyrite surface, which was then exposed to air, and subsequently left in water for 10 min. At each stage of this procedure, the sample was reintroduced into the UHV system, and photoemission and XANES measurements were performed. The sample was then removed for subsequent treatment. The low-binding energy (defect) feature attributed to monosulfide is lost upon exposure to air, and a significant amount of sulfate is produced on the surface in the course of 40 h reaction in air. Following 10 min in water, the majority of this sulfate has been lost from the surface into solution.

In Figure 6 we show both S 2*p* (a) and Fe 2*p* (b) photoemission results for a series of 5 min reactions in chromium-free water of varying pH. These data show that there is little evidence of reaction products observable at the pyrite surface, which we attribute to removal of soluble species as discussed above, especially under acidic conditions.

Figure 7 shows the results of curve fitting of a S 2*p* photoemission spectrum collected from a chromium-reacted surface, that, following the subtraction of a linear and integrated (Shirley) background, can be deconvolved into at least 5 Voigt components. The S $2p_{3/2}$ binding energies of these features, along with their shift from the bulk disulfide in pyrite, are as follows: surface disulfide, 161.8 eV (−0.6); bulk disulfide, 162.4 eV (0); elemental sulfur or polysulfide, 164.1 eV (+1.7); sulfite, 166.7 eV (+4.3); and sulfate, 168.6 eV (+6.2). The trapped oxidation products S^0, SO_3, and SO_4 are present in the approximate ratio of 1:5:4. Spectral fitting was performed using the Aanalyzer® program (Herrera-Gómez et al., 2000). These assignments are in good agreement with those already published (Lindberg et al., 1970; Schaufuβ et al., 1998a; Schaufuβ et al., 1998b; Smart et al., 1999; Descostes et al., 2000). It should be noted that the full width at half maximum (FWHM) of the peaks fitting the S(−1) and S(0) species were narrow, whereas the S(IV) and S(VI) species were fitted with broader envelopes. The reason for the broadness of these features may be attributable to a number of factors, including disorder on the surface and a variety of chemical environments for each formal sulfur oxidation state due to varying degrees of hydration of these moieties. The existence of a variety of sulfur oxidation states on the surface is consistent with a number of previous studies on arsenopyrite and gersdorffite (Schaufuß et al., 2000; Nesbitt et al., 2003) that demonstrate stepwise addition of oxygen to sulfur centers.

For doses at pH 7 with 50 μM Cr(VI) there is little increase in the quantity of oxidized sulfur observed beyond 5 min exposure, and indeed less in some instances. Because oxidation continues during this time, we attribute the lack of oxidized sulfur species to their dissolution from the surface. In contrast, the 30 s dose with 5 mM Cr(VI) reacts rapidly relative to the rate of dissolution of soluble oxidation products, such that sulfoxy species are trapped at the surface within the reduced chromium coating.

3.2.3. Iron 2p photoemission and L-edge X-ray absorption data

Figure 8 shows Fe 2*p* photoemission, while Figure 9 shows Fe L_{II},L_{III}-edge XANES spectra for the Cr(VI) dosing regimes. For comparison, the photoemission and adsorption spectra from a pyrite surface treated with 0.6% w/w hydrogen peroxide is also shown as an example of an oxidized pyrite surface containing both Fe(II) and Fe(III). The main feature in the photoemission spectra is the bulk Fe(II) signal at approximately 707 eV ($2p_{3/2}$), that exhibits a tail to high-binding energies. The tail has been attributed to Fe(II)-S and Fe(III)-S surface states (Nesbitt et al., 2000). At pH 2, there is no photoemission evidence for a Fe(III)-O surface state, which is normally centered around 710 to 712 eV (McIntyre and Zetaruk, 1977) on the pyrite surface; however, at both pH 4 and pH 7 there is a shoulder shifted from the Fe(II) signal by ca. 4 eV, that indicates a small quantity of Fe(III) coordinated by oxygen on the pyrite surface.

The speciation of iron was confirmed using Fe L_{II},L_{III}-edge XANES, which is displayed in Figure 9. At first glance it

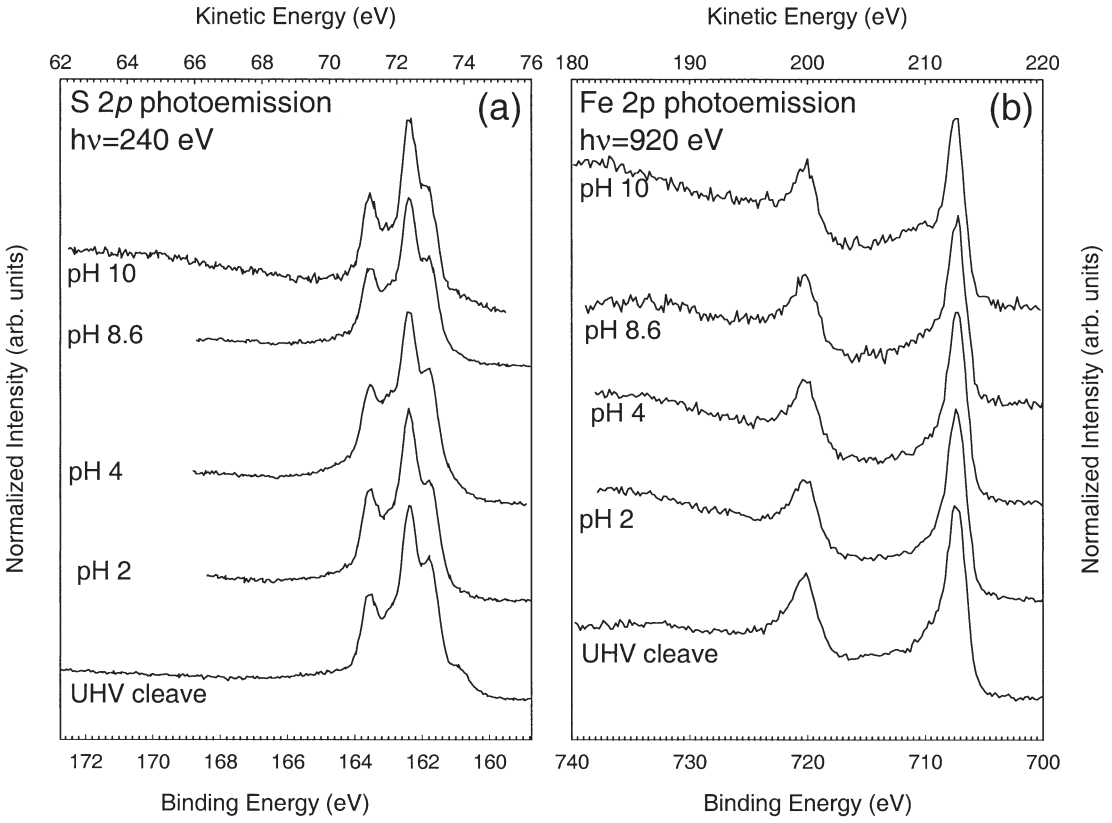

Fig. 6. S 2*p* (a) and Fe 2*p* (b) photoemission from pyrite surfaces reacted with water for 5 min over the range of pH used in chromate-dosing experiments.

appears that there is no difference in the L_{II},L_{III}-edges. However, there is a subtle change in the shape of the L_{III}-edge, which is manifested most clearly as an increase in intensity on the high energy side of the L_{III}-edge. This feature is most prominent in the spectrum of the hydrogen peroxide-treated surface, which shows significant contributions from both iron(II) and iron(III). This high energy shoulder confirms the presence of iron(III) on the pyrite surface, as suggested from the XPS data. The formation of iron(III) at the surface should also result in an increase in the branching ratio, $I(L_{III})/\{I(L_{II})+I(L_{III})\}$ (Thole and Van der Laan, 1988) as iron changes from low-spin Fe(II) to high-spin Fe(III). Comparison of the iron L_{II},L_{III}-edges collected in TEY and the more surface-sensitive AEY modes show that the intensity of the L_{II} edge is slightly lower in the AEY mode. Thus there is an increase in the branching ratio at the surface relative to the more bulk sensitive TEY measurement, which combined with the XPS data, provides strong evidence that there is Fe(III) on pyrite surfaces following reaction with chromate at circumneutral pH for both high- and low-chromate concentrations.

3.2.4. Oxygen K-edge X-ray absorption

Oxygen *K*-edge X-ray absorption provides a convenient and complementary probe for the speciation of oxidized pyrite surfaces. A recent study of the oxidation of pyrite surfaces by air-saturated aqueous solutions (pH 3–10) and by aqueous iron(III) by Todd et al. (2003b) made extensive use of this technique for identification of oxygen-containing species at the pyrite surface. The oxygen species present were found to vary with pH, from iron(III)-oxyhydroxide at alkaline pH, to a mixture of iron(III)-oxyhydroxide and iron(III)-(hydroxy)sulfate under circumneutral pH conditions (Todd et al., 2003b).

Further evidence for the formation of a metal (oxy)hydroxide overgrowth on Cr(VI)-reacted pyrite is provided by the O *K*-edge XANES data shown in Figure 10. These data show Auger- and total-electron yield spectra for a series of Cr(VI) doses at pH 7 ranging from 1 to 60 min with 50 μM Cr(VI) and 30 s with 5 mM. The oxygen *K*-edge spectra are complicated by the fact that there are most likely a number of oxygen-containing species at the surface. As such there could be contributions from sulfur oxoanions, iron, and/or chromium (oxy)hydroxides, and chromium oxoanions. All data, with the exception of the 30 s 5 mM dose (top spectrum), were from samples that showed only Cr(III) on the surface. Figure 11 presents O *K*-edge spectra of a number of model compounds that aid our interpretation of the O *K*-edge data presented in Figure 10.

Of particular importance to our interpretation is the preedge feature labeled 'C', which is indicative of hydroxyl groups (Kendelewicz et al., 2000) and increases with increasing Cr(VI) dosing time. The presence of this feature supports our hypothesis of the buildup of a chromium(III)-(oxy)hydroxide layer. The features labeled 'A' and 'B' in the upper spectrum are due to 1*s* to e_g and 1*s* to t_{2g} transitions in the CrO_4^{2-} anion (Brydson

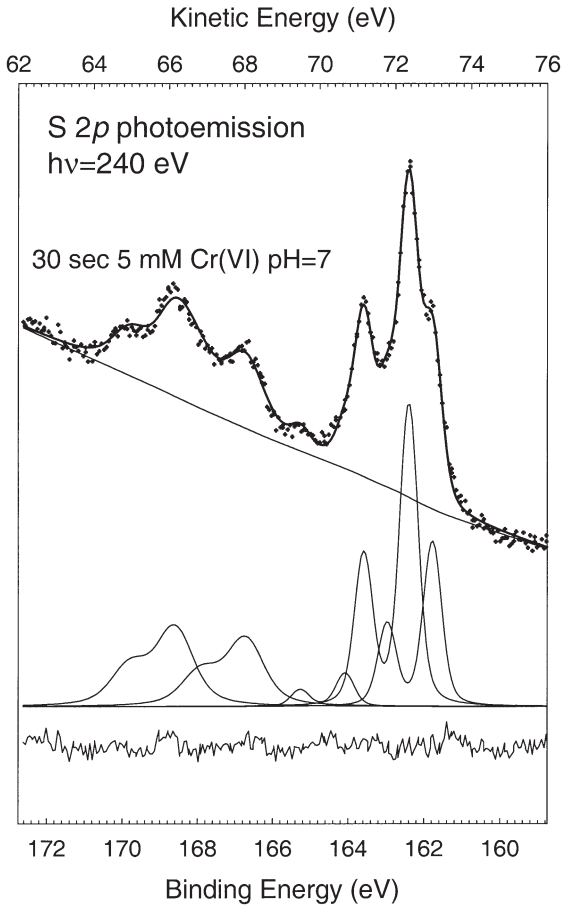

Fig. 7. Fitting of the surface sensitive S 2*p* photoemission from a pyrite surface following reaction for 30 s with 5 mM Cr(VI) at pH 7. The experimental data are represented by points, the calculated fit by a solid line, and the baseline, individual components, and residual by fine solid lines. This fit is representative of those for our S 2*p* data.

et al., 1993), and thus this spectrum is the sum of contributions from the chromate anion and from an underlying chromium (oxy)hydroxide layer.

The spectroscopic signature of hydroxyls in the oxygen *K*-edge has been somewhat controversial (Wirth, 1997; van Aken et al., 1998; Wirth, 1998), and in the following discussion we present evidence for such a spectroscopic signature in this system and use it in the interpretation of the data contained in Figure 10.

The O *K*-edge adsorption process involves the promotion of a core-level electron ($l = 0$) into unoccupied oxygen or continuum states with *p* character ($l = 1$) in the vicinity of the excited atom, which can couple to the core level through the dipole selection rule (Stöhr, 1988). Much attention has been placed on the O *K*-edge spectra of transition metal oxides, and Chen (1997) provides a thorough review of these studies. It is convenient to consider the oxygen *K*-edge as consisting of two regions. The first region, referred to as the preedge, is attributed to O 2*p* character in predominantly metal 3*d* orbitals and lends itself to molecular orbital treatment. The second region, which is at higher energy, is not so readily described using a molecular orbital approach (de Groot et al., 1989), and a better description of this region is obtained using band structure methods (de Groot et al., 1993) or multiple scattering calculations (Wu et al., 1997). In the case of transition metal oxides, the oxygen 2*p* states are fully occupied in a simple ionic picture, and weak, if any, absorption is expected. However, covalent mixing of the oxygen *s* and *p* states with the metal *d* states lifts the selection rule and produces states of mixed *p*-d character, which vary with coordination geometry and are manifested as generally sharp resonances in the adsorption edge before the continuum states and ionization potential. For octahedral coordination, such as in iron, or chromium oxides, or oxyhydroxides, the resulting molecular orbitals are filled to the t_{1g} (π) level; four unoccupied hybridized levels remain, which, in order of increasing energy, have symmetry labels t_{2g} (π^*), e_g (σ^*), a_{1g} (σ^*), and t_{1u} (σ^*, π^*). Tetrahedral coordination changes the ordering of energy levels somewhat, with the highest occupied molecular orbital now being t_1 and the unoccupied molecular orbitals are e, t_2, t_2, and a_1 (Ballhausen and Gray, 1965; Huheey, 1983). Figure 12 shows simplified molecular orbitals for transition metal ions in both octahedral (after Chen (1997)) and tetrahedral (after Brydson et al. (1993))

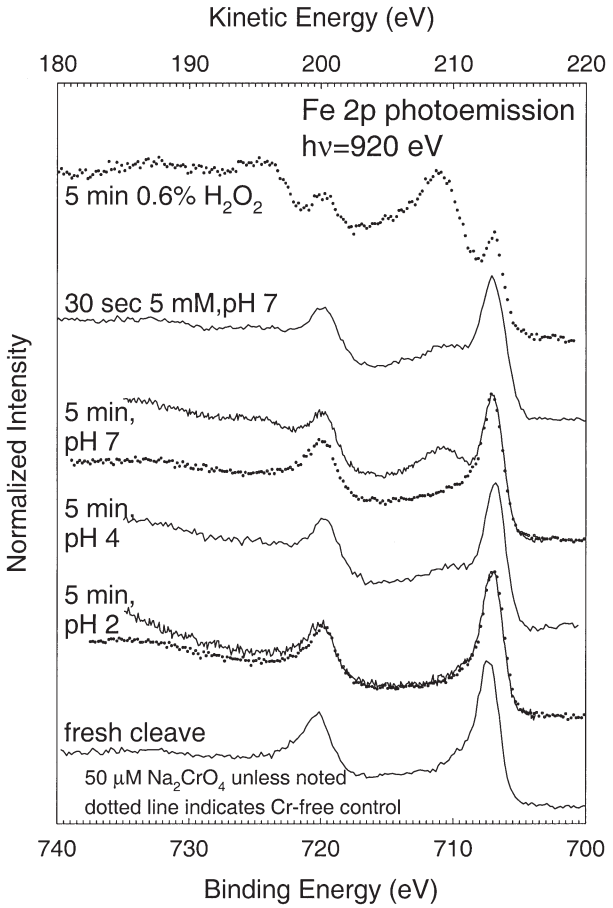

Fig. 8. Surface sensitive Fe 2*p* photoemission from pyrite surfaces following 5 min reaction with 50 μM Cr(VI) solution at pH 2, pH 4, and pH 7, and 30 s with 5 mM Cr(VI) at pH 7. Spectra for Cr-free solutions under similar pH conditions are included as broken lines, and the spectrum of a UHV-fractured surface is also shown for comparison. A spectrum from a heavily oxidized pyrite surface (5 min in 0.6% w/w hydrogen peroxide) is also included.

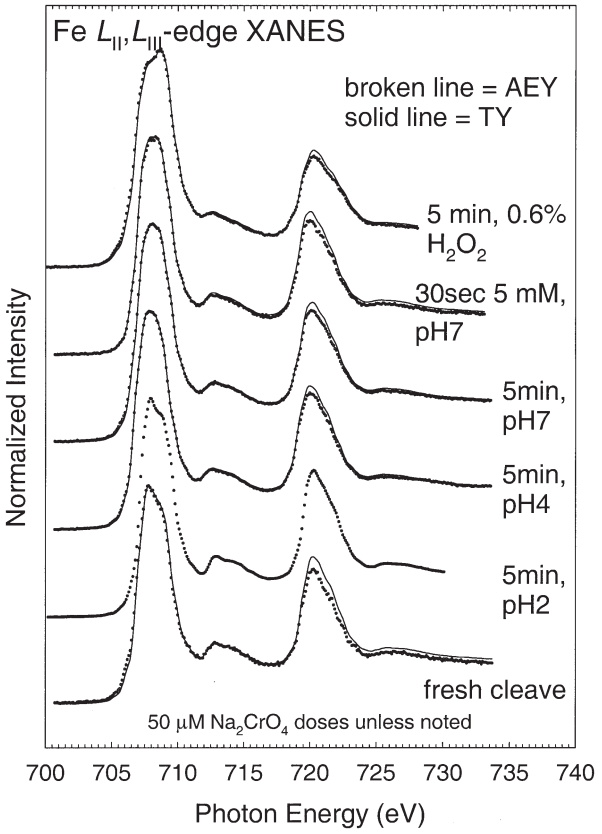

Fig. 9. Iron L_{II},L_{III}-edge XANES from pyrite surfaces following 5 min reaction with 50 μM Cr(VI) solution at pH 2, pH 4, and pH 7, and 30 s with 5 mM Cr(VI) at pH 7. Solid lines indicate Auger electron yield data, and broken lines are total electron yield data. A spectrum from a heavily oxidized pyrite surface (5 min in 0.6% w/w hydrogen peroxide) is also included.

oxygen coordination. Filled orbitals on this diagram correspond to $[FeO_6^{9-}]$ and $[CrO_4^{2-}]$. This model allows for the interpretation of the preedge features labeled 'A' and 'B' in the manganite, goethite, and hematite spectra as transitions from the O1*s* to t_{2g} and e_g molecular orbitals, with the splitting between these orbitals approximately 1.4 eV. In crocoite these features arise from 1*s* to e and t_2 orbital transitions, with a splitting of approximately 1.2 eV.

In Figure 11 we present data for goethite, limonite ($FeOOH \cdot nH_2O$), and manganite (γ-MnOOH), which all show a third feature, 'C', approximately 1.4 eV above feature 'B'. We believe that the origin of this feature is analogous to that of feature 'B', in that it is a 1*s* to e_g transition; however, the 1*s* core level of an hydroxide oxygen in goethite is shifted by approximately 1.4 eV to higher binding energy with respect to an oxide oxygen—a value that is typical of iron oxides (Brundle et al., 1977; McCafferty et al., 1988; Kendelewicz et al., 2000). Crystal field splittings, which are approximately equal to the e_g-t_{2g} splitting, range from approximately 2.5 eV for early first-row transition metals to 1.2 eV for late first-row transition metals (de Groot et al., 1989). For the iron oxyhydroxides goethite and lepidocrocite, the splittings are 1.9 eV, and 2.0 eV, respectively (Sherman and Waite, 1985). The comparable magnitude of the crystal field splitting and the O 1*s* binding energy shift result in the superposition of the 1*s* to t_{2g} transition arising from hydroxyl oxygens with the 1*s* to e_g transition from oxide oxygens. This results in a three-peak structure as is observed for goethite, limonite, and manganite. It is interesting to note that feature 'C', which we attribute to hydroxyl, is strongest in limonite—a phase which while not a mineral in the true sense, is a mixture of hydrated iron oxyhydroxide and hydroxide phases, with appreciable water content (Klein and Hurlbut, 1993). Van Aken et al. (1998) present O *K*-edge data for lepidocrocite (γ-FeOOH) and hematite (α-Fe_2O_3), both of which show two features analogous to those labeled 'A' and 'B', however the hydroxyl feature 'C' was not observed, and the spectrum looks remarkably like the O *K*-edge ELNES spectrum of a maghemite (γ-Fe_2O_3) powder published by Norrish and Smith (1975). Lepidocrocite dehydroxylates to hematite via maghemite (Waychunas, 1991; Cornell and Schwertmann, 1996), and this may account for the difference between our measurements of hydroxyl-containing species such as goethite, limonite, and manganite, which show a third feature, and the spectrum of lepidocrocite presented by van Aken et al. (1998), which does not.

The prominent preedge features observed for the transition metal oxides and oxyhydroxides due to transitions to metal 3*d* states with ligand *p*-character are much weaker in the oxygen *K*-edge adsorption of the sulfate anion. As the bonding in a

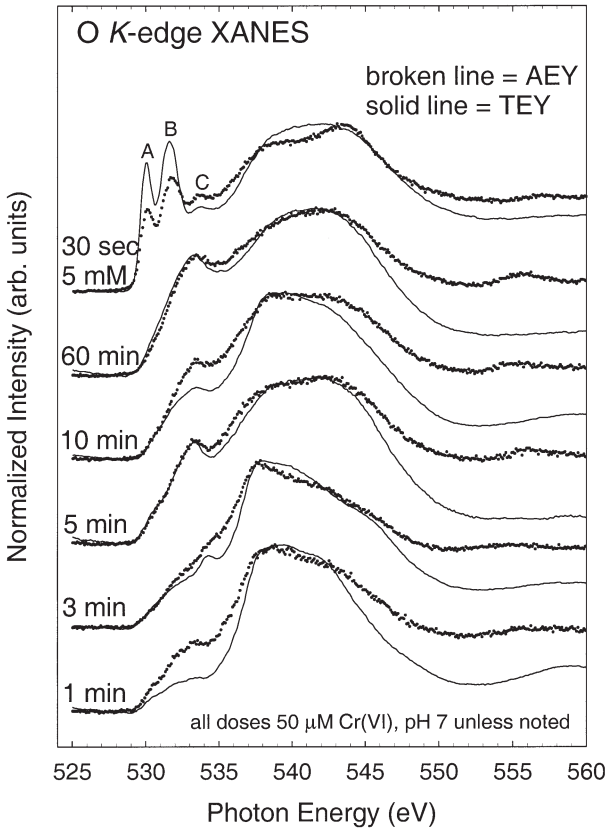

Fig. 10. Oxygen *K*-edge XANES of freshly fractured pyrite surfaces reacted with 50 μM Cr(VI) solutions at pH 7 for reaction times between 1 min and 1 hr, along with data for pyrite reacted for 30 s with 5 mM Cr(VI) at pH 7. Solid lines indicate Auger electron yield data, and broken lines are total electron yield data.

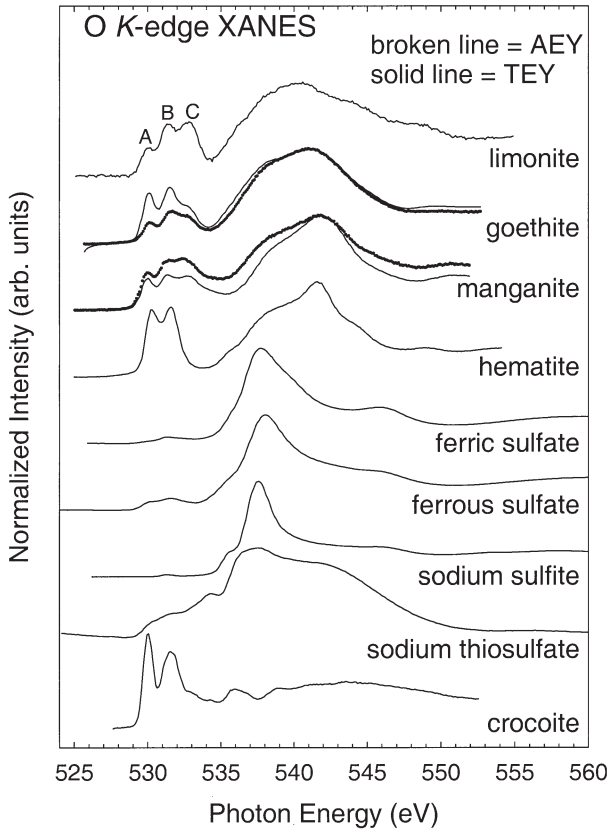

Fig. 11. Oxygen *K*-edge XANES of model compound for oxygen in a variety of coordination environments. Data are included for oxide, oxyhydroxide, sulfoxy, and oxoanion species. Solid lines indicate Auger electron yield data, and broken lines are total electron yield data.

material becomes more ionic, there is a decrease in the number of available metal 3*d* states with ligand 2*p* character, and thus a decrease in the O 1*s* signal at threshold (Sherman, 1985a; Sherman, 1985b; de Groot et al., 1989) due to closure of the 1*s* to n*p* channel. This increase in ionic bonding character leads to much weaker preedge resonances observed for ferric or ferrous sulfate (Kelty et al., 1999; Todd and Sherman, 2003; Todd et al., 2003a; Todd et al., 2003b). The bonding in sulfite and thiosulfate also involves similar ionicity and thus little preedge structure is expected. The O *K*-edge spectra shown in Figure 11 reflect this. The data for sulfate is in excellent agreement with that published previously (Kelty et al., 1999). The question arises as to whether the adsorption from an ion in a crystallized model compound reflects that same ion when adsorbed to a mineral surface. Ab initio calculations of the adsorption geometry of sulfate on silver and gold surfaces indicate that the Highest Occupied Molecular Orbitals (HOMOs) of sulfate are nonbonding orbitals of predominantly O *s* and *p* character, while the Lowest Unoccupied Molecular Orbitals (LUMOs) have strong sulfur contributions and consist of σ^*, π^*, and σ^* orbitals (Patrito et al., 1997). Bonding of the sulfate anion to the gold and silver surfaces is via donation of σ electron density, with some back donation from the metal *s* and *p* states, which leaves the surface complex electronically similar to the unbound sulfate.

The changes occurring in the O *K*-edge data presented in Figure 10 can be interpreted as being due to predominantly hydroxyl-containing species with sulfoxy contributions. The upper spectrum also contains contributions from the chromate anion, as discussed above. The growth of the feature 'C' is interpreted as being due to increasing hydroxyl-containing species on the surface. If the hydroxyl containing species were an

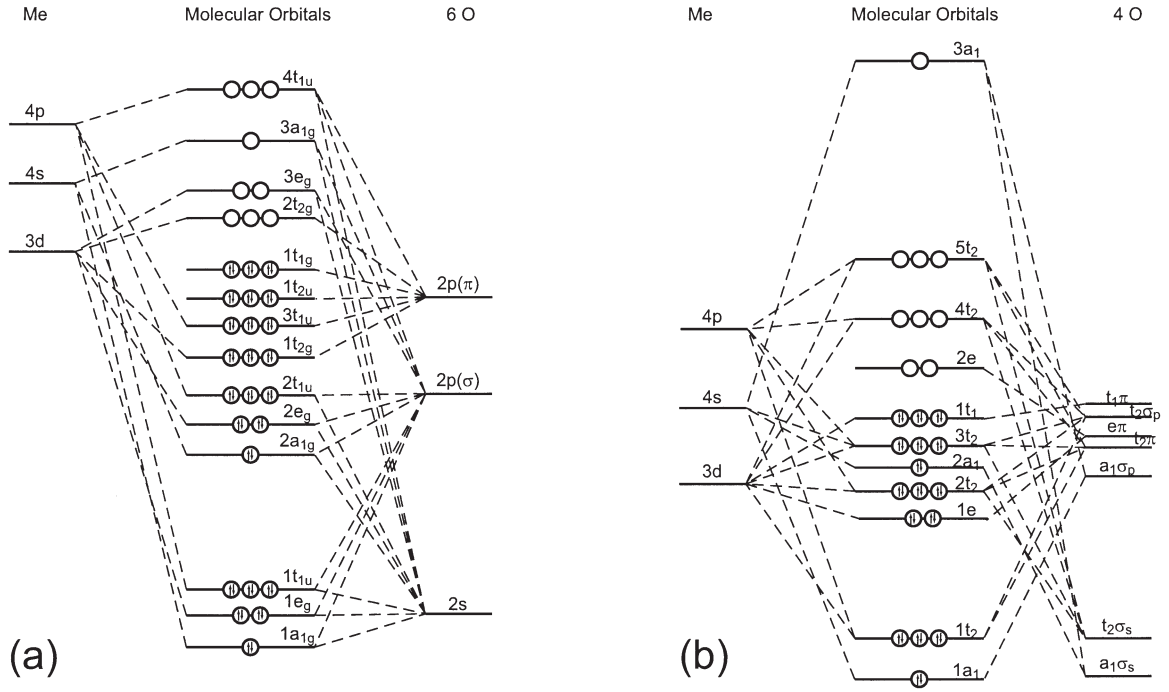

Fig. 12. Molecular orbital diagrams for (a) MO_6 (after Chen (1997)) and (b) MO_4 (after Brydson et al. (1993)) coordination environments. Filled orbitals on this diagram correspond to $[FeO_6^{9-}]$ and $[CrO_4^{2-}]$.

iron oxyhydroxide, then the features 'A' and 'B' at 530 and 531.5 eV from the O^{2-} component should also be apparent. The absence of the doublet, or triplet, structure in the O preedge region, we feel, discounts the possibility that the surface species is an iron hydroxide or oxyhydroxide. The O *K*-edge spectrum of CrOOH is described by Schedel-Niedrig (1996) as consisting of a weak white line at 533 eV. A multiple peak structure as in the iron oxides is not expected for a high-spin d^3 species such as Cr(III), as the *d* manifold is further modified by exchange splitting, resulting in a superposition of the e_g^{α} and t_{2g}^{β} states (de Groot et al., 1989). When combined with the XPS data which show an increase in chromium(III) at this surface along with an increase in feature 'C' at 533 eV, we feel confident in asserting that the dominant species on the surface is a chromium oxyhydroxide species.

Our oxygen *K*-edge spectra for chromate-oxidized pyrite surfaces differ from those recently collected from oxidized pyrite surfaces by Todd et al. (2003b). The difference is due to the composition of the oxidized surface, which in this case is predominantly chromium(III) oxyhydroxide, whereas in the absence of Cr(VI) in solution, a surface layer consisting of iron (III) oxyhydroxide and iron (III) hydroxysulfate results (Todd et al., 2003b).

3.3. Reaction Mechanism of the Chromate-Pyrite Reaction

The spectral data discussed above can be used to refine a mechanistic model of pyrite oxidation by chromate. We believe our results are consistent with the currently accepted models of pyrite oxidation (e.g., Luther, 1990; Nordstrom and Alpers, 1999), where dissolution of Fe(II) leads to Fe(III) in solution, which then attacks the S_2^{2-} producing SO_4^{2-} and Fe(II). The Fe(II) cycles to Fe(III) and the reaction propagates. It appears that Cr(VI) oxidizes Fe(II) centers on the pyrite surface and increases the amount of Fe(III) available for the oxidation of the disulfide group. Chromate could influence the oxidation of pyrite in three possible ways: (i) oxidation of the Fe(II) to Fe(III) on the pyrite surface with the thus liberated Fe(III) then acting as the oxidizing agent towards disulfide according to reaction (4); (ii) via electron transfer from Cr(VI) directly to the S_2^{2-} group, or (iii) by a combination of (i) and (ii). Rosso et al. (1999a; 1999b) indicate that redox reactions should preferentially proceed via iron sites at the pyrite surface as both the HOMO and LUMO on the {100} pyrite surface are nonbonding levels dominated by Fe 3*d* character. Reaction with O_2 leads to oxidative consumption of the occupied dangling bond states localized on surface iron atoms, and the formation of Fe–O bonds. This tends to discount the possibility of direct electron transfer between chromate and disulfide groups. Reduction of chromate to Cr(III) involves the transfer of three electrons to the chromium center. Peterson et al. (1997) showed that on magnetite, the three electrons come from three Fe(II) centers. Benincasa et al. (2002) recently studied the oxidation of pyrite using Cr(VI) as an oxidizing agent and report the following overall reaction (ignoring hydrolysis of Cr^{3+}):

$$2FeS_2 + 5Cr_2O_7^{2-} + 32H^+ \rightarrow 2Fe(OH)_3 + 4SO_4^{2-} + 10Cr^{3+} + 13H_2O \quad (6)$$

This reaction stoichiometry implies that Cr(VI) oxidizes both Fe(II) and S_2^{2-}. In the present study we find no clear evidence for this reaction pathway. Instead, we propose that Cr(VI) reacts with Fe(II) at the pyrite surface, resulting in the release of three Fe(III) into solution.

$$3FeS_2 + CrO_4^{2-} + 8H^+ \rightarrow 3Fe^{3+} + 3S_2^{2-} + Cr^{3+} + 4H_2O \quad (7)$$

The Fe(III) can then oxidize the pyrite disulfide group via the pathway indicated in reaction (4), which leads to:

$$42Fe^{3+} + 3S_2^{2-} + 24H_2O \rightarrow 42Fe^{2+} + 6SO_4^{2-} + 48H^+ \quad (8)$$

Combining reactions (7) and (8) leads to an overall reaction

$$3FeS_2 + CrO_4^{2-} + 39H^+ + 20H_2O \rightarrow Cr^{3+} + 42Fe^{2+} + 6SO_4^{2-} + 40H^+ \quad (9)$$

As noted previously, as oxidation of the pyrite surface proceeds, a change in the surface charging occurs as the surface alters from pristine pyrite to an iron(III) oxide-like phase. This is accompanied by a change in the surface charge at the mineral-water interface from positive, when the pH is above pH_{PZC} of pyrite, to negative when the pH is below the pH_{PZC} of iron oxides. Such charging behavior may have important implications for pyrite oxidation by chromate because the chromate anion must overcome repulsion by the negatively charged surface to be reduced at the surface of pyrite. Indeed, chromate sorption experiments on the magnetite (111) surface showed a marked decrease in chromium reduction when the solution pH was above the pH_{PZC} of the magnetite surface (Kendelewicz et al., 2000). Our proposed mechanism is not dependent on these charging effects, in that chromate reacts with a cation, potentially in solution, to generate a reactive cationic species that would be attracted to the negatively charged pyrite surface.

4. SUMMARY AND CONCLUSIONS

These studies show that chromate is an effective oxidizing agent for the pyrite surface, and conversely that pyrite can be used as a means of reductively immobilizing chromate. When the chromate solution concentration is 50 μM, the coating does not inhibit further oxidation of the pyrite surface, on the timescale of these experiments, and all chromium present on the pyrite surface is in the reduced Cr(III) form. At a chromate concentration of 5 mM, the pyrite surface becomes rapidly coated with an Fe(III)- and Cr(III)-containing phase which prevents complete chromium reduction, and unreduced chromate is adsorbed on the Cr(III) coating. We attribute this differing behavior to kinetic effects. At the higher chromate concentrations, oxidized sulfur species are retained at the pyrite surface. At high Cr(VI) concentrations, these oxidized sulfur species (and chromate) appear to be trapped in an oxidized surface overlayer because the rate of deposition of $Cr(OH)_3$ exceeds the rate of removal of oxidized sulfur species. In contrast, the removal of soluble oxidized species into solution regenerates reactive pyrite surfaces, which allows the reaction to proceed at lower Cr(VI) concentrations. Sulfur 2*p* photoemission identified sulfate, sulfite, and zero-valent sulfur on the pyrite surface. The features due to sulfate and sulfite are broad

and were fit using a single broad envelope, which may include contributions from disorder and varying degrees of hydration. Iron 2*p* photoemission and *L*-edge XANES show that only minor amounts of iron (III) remain on the surface, indicating that the majority of this species is rapidly lost into solution. The chromate was reductively sorbed onto the pyrite surface forming an (oxy)hydroxide layer which, at high chromate concentrations, passivates the surface towards chromium reduction. The presence of unreduced chromate on the Cr(III)-(oxy)hydroxide layer that was rapidly formed from high chromate concentration in solution was confirmed by both Cr *L*-edge and O *K*-edge XANES. Oxygen-containing species present on the surface of oxidized pyrite were identified as sulfoxy and hydroxyl functional groups. It appears that the proportion of hydroxyl species at (or near) the surface increases with time. Changes in species concentration over time suggests the steady state production and loss of oxidized sulfoxy species at the surface along with the deposition of a predominantly Cr(III) hydroxide phase. We find no evidence to suggest that chromate is a direct oxidant for the pyrite disulfide group and believe that the role of chromate is in oxidation of Fe(II) in pyrite to Fe(III), either in solution or at the pyrite surface, which then is the oxidant of the disulfide group.

Acknowledgments—We gratefully acknowledge financial support from the National Science Foundation through the NSF-CRAEMS Program (Grant CHE 0089215) and from the Department of Energy, Environmental Molecular Science Program (Grant DE-FG07–99ER15024). Portions of this research were carried out at the Stanford Synchrotron Radiation Laboratory, a national user facility operated by Stanford University on behalf of the U.S. Department of Energy, Office of Basic Energy Sciences. Technical support from the staff of the Stanford Synchrotron Radiation Laboratory, and in particular Britt Hedman and the SSRL Biotech Program for providing additional beamtime to complete the experimental work reported herein, is also gratefully acknowledged. We would like to thank D. J. Vaughan for editorial handling, and H. W. Nesbitt and an anonymous reviewer for help in improving this manuscript.

Associate editor: D. J. Vaughan

REFERENCES

Ballhausen C. J. and Gray H. B. (1965) *Molecular Orbital Theory: An Introductory Lecture Note and Reprint Volume*. W. A. Benjamin, Inc.

Bebie J., Schoonen M. A. A., Fuhrmann M., and Strongin D. R. (1998) Surface charge development on transition metal sulfides: An electrokinetic study. *Geochim. Cosmochim. Acta* **62,** 633–642.

Benincasa E., Brigatti M. F., Franchini G., Malferrari D., Medici L., Poppi L., and Tonelli M. (2002) Reactions between Cr(VI) solutions and pyrite. Chemical and surface studies. *Geologica Carpathica* **53,** 79–85.

Bonnissel-Gissinger P., Alnot M., Ehrhardt J.-J., and Behra P. (1998) Surface oxidation of pyrite as a function of pH. *Environ. Sci. Technol.* **32,** 2839–2845.

Boursiquot S., Mullet M., and Ehrhardt J.-J. (2002) XPS study of the reaction of chromium (VI) with mackinawite (FeS). *Surf. Interface Anal.* **34,** 293–297.

Bronold M., Tomm Y., and Jagermann W. (1994) Surface states on cubic d-band semiconductor pyrite (FeS_2). *Surf. Sci.* **314,** L931–L936.

Brundle C. R., Chuang T. J., and Wandelt K. (1977) Core and valence level photoemission studies of iron oxide surfaces and the oxidation of iron. *Surf. Sci.* **68,** 459–468.

Brydson R., Garvie L. A. J., Craven A. J., Sauer H., Hofer F., and Cressey G. (1993) *L.* 2, 3. edges of tetrahedrally coordinated d^0 transition-metal oxyanions XO_4^{n-}. *J. Phys.: Condens. Matter.* **5,** 9379–9392.

Chen J. G. (1997) NEXAFS investigations of transition metal oxides, nitrides, carbides, sulfides and other interstitial compounds. *Surf. Sci. Rep.* **30,** 1–152.

Chirita P. (2003) Kinetics of aqueous pyrite oxidation by potassium dichromate - An experimental study. *Turk. J. Chem.* **27,** 111–118.

Cornell R. M. and Schwertmann U. (1996) *The iron oxides: structure, properties, reactions, occurrences and uses.* VCH, New York. Wiley-VCH Publishers.

Cotton F. A. and Wilkinson G. (1988) Advanced Inorganic Chemistry: A Comprehensive Text. John Wiley & Sons, Inc.

de Groot F. M. F. (1994) X-ray absorption and dichroism of transition metals and their compounds. *J. Elec. Spec. Rel. Phenom.* **67,** 529–622.

de Groot F. M. F., Grioni M., Fuggle J. C., Ghijsen J., Sawatzky G. A., and Petersen H. (1989) Oxygen 1*s* x-ray-absorption edges of transition-metal oxides. *Phys. Rev. B.* **40,** 5715–5723.

de Groot F. M. F., Faber J., Michiels J. J. M., Czyzyk M. T., Abbate M., and Fuggle J. C. (1993) Oxygen 1*s* x-ray absorption of tetravalent titanium oxides: A comparison with single-particle calculations. *Phys. Rev. B.* **48,** 2074–2080.

Descostes M., Mercier F., Thromat N., Beaucaire C., and Gautier-Soyer M. (2000) Use of XPS in the determination of chemical environment and oxidation state of iron and sulfur samples: constitution of a data basis in binding energies for Fe and S reference compounds and applications to the evidence of surface species of an oxidised pyrite in a carbonate medium. *App. Surf. Sci.* **165,** 288–302.

Eggleston C. M., Ehrhardt J.-J., and Stumm W. (1996) Surface structural controls on pyrite oxidation kinetics: An XPS-UPS, STM, and modeling study. *Am. Mineral.* **81,** 1036–1056.

Evangelou V. P. and Zhang Y. L. (1995) A review: pyrite oxidation mechanisms and acid mine drainage prevention. *Crit. Rev. Environ. Sci. Technol.* **25,** 141–199.

Fornasiero D., Eijt V., and Ralston J. (1992) An electrokinetic study of pyrite oxidation. *Colloids Surf.* **62,** 57–61.

Goldhaber M. B. (1983) Experimental study of metastable oxyanion formation during pyrite oxidation at pH 6–9 and 30°C. *Am. J. Sci.* **283,** 193–217.

Guevremont J. M., Elsetinow A. R., Strongin D. R., Bebie J., and Schoonen M. A. A. (1998a) Reactivity of the (100) Plane of Pyrite in Oxidizing Gaseous and Aqueous Environments: Effect of Surface Imperfections. *Environ. Sci. Technol.* **32,** 3743–3748.

Guevremont J. M., Elsetinow A. R., Strongin D. R., Bebie J., and Schoonen M. A. A. (1998b) Structure sensitivity of pyrite oxidation: comparison of the (100) and (111) planes. *Am. Mineral.* **83,** 1353–1356.

Herrera-Gómez A., Pianetta P., Marshall D., Nelson E., and Spicer W. E. (2000) Geometrical structure of the 1/2-ML (2×1) and 1/3-ML (2×3) Ba/Si(001) interfaces. *Phys. Rev. B.* **61,** 12988–12991.

Huheey J. E. (1983) *Inorganic Chemistry: Principles of Structure and Reactivity*. Harper & Row.

Kelty S. P., Li J., Chen J. G., Chianelli R. R., Ren J., and Whangbo M.-H. (1999) Characterization of the RuS_2(100) Surface by Scanning Tunneling Microscopy, Atomic Force Microscopy, and Near-Edge X-ray Absorption Fine Structure Measurements and Electronic Band Structure Calculations. *J. Phys. Chem. B.* **103,** 4649–4655.

Kendelewicz T., Liu P., Doyle C. S., Brown G. E., Jr, Nelson E. J., and Chambers S. A. (1999) X-ray adsorption and photoemission study of the adsorption of aqueous Cr(VI) on single crystal hematite and magnetite surfaces. *Surf. Sci.* **424,** 219–231.

Kendelewicz T., Liu P., Doyle C. S., and Brown G. E., Jr.. (2000) Spectroscopic study of the reaction of aqueous Cr(VI) with Fe_3O_4 surfaces. *Surf. Sci.* **469,** 144–163.

Kim J. G., Jung P.-K., Moon H.-S., and Chon C.-M. (2002) Reduction of hexavalent chromium by pyrite-rich andesite in different anionic solutions. *Environ. Geol.* **42,** 642–648.

Klein C. and Hurlbut C. S., Jr.. (1993) Manual of Mineralogy. John Wiley & Sons.

Laajalehto K., Kartio I., and Suoninen E. (1997) XPS and SR-XPS techniques applied to sulphide mineral surfaces. *Int. J. Miner. Process.* **51,** 163–170.

Lindberg B. J., Hamrin K., Johansson G., Gelius U., Fahlman A., Nordling C., and Siegbahn K. (1970) Molecular spectroscopy by means of ESCA. II. Sulfur compounds. Correlation of electron binding energy with structure. *Phys. Scr.* **1,** 286–298.

Liu P., Kendelewicz T., Brown G. E., Jr, and Parks G. A. (1998) Reaction of water with MgO(100) surfaces. Part I: Synchrotron X-ray photoemission studies of low-defect surfaces. *Surf. Sci.* **412/413,** 287–314.

Lowson R. T. (1982) Aqueous oxidation of pyrite by molecular oxygen. *Chem. Rev.* **82,** 461–497.

Luther G. W., III.. (1987) Pyrite oxidation and reduction: Molecular orbital theory considerations. *Geochim. Cosmochim. Acta* **51,** 3193–3199.

Luther G. W., III.. (1990) The Frontier-Molecular-Orbital Theory Approach in Geochemical Processes. In *Aquatic Chemical Kinetics: Reaction Rates of Processes in Natural Waters, Environmental Science and Technology* (ed. W. Stumm), pp. 173–198. John Wiley & Sons, Inc.

Luther G. W., III.. (1997) Comment on "Confirmation of a sulfur-rich layer on pyrite after oxidative dissolution by Fe(III) ions around pH 2" by K. Sasaki et al. *Geochim. Cosmochim. Acta* **61,** 3269–3271.

McCafferty E., Bernett M. K., and Murday J. S. (1988) An XPS study of passive film formation on iron in chromate solutions. *Corros. Sci.* **28,** 559–576.

McIntyre N. S. and Zetaruk D. J. (1977) X-ray photoelectron spectroscopic studies of iron oxides. *Anal. Chem.* **49,** 1521–1529.

McKibben M. A. and Barnes H. L. (1986) Oxidation of pyrite in low temperature acidic solutions: Rate laws and surface textures. *Geochim. Cosmochim. Acta* **50,** 1509–20.

Moses C. O., Norstrom D. K., Herman J. S., and Mills A. L. (1987) Aqueous pyrite oxidation by dissolved oxygen and by ferric ions. *Geochim. Cosmochim. Acta* **51,** 1561–1571.

Nesbitt H. W. and Muir I. J. (1994) X-ray photoelectron spectroscopic study of a pristine pyrite surface reacted with water vapor and air. *Geochim. Cosmochim. Acta* **58,** 4667–4679.

Nesbitt H. W., Bancroft G. M., Pratt A. R., and Scaini M. J. (1998) Sulfur and iron surface states on fractured pyrite surfaces. *Am. Mineral.* **83,** 1067–1076.

Nesbitt H. W., Scaini M., Höchst H., Bancroft G. M., Schaufuss A. G., and Szargan R. (2000) Synchrotron XPS evidence for Fe^{2+}-S and Fe^{3+}-S surface species on pyrite fracture-surfaces, and their 3D electronic states. *Am. Mineral.* **85,** 850–857.

Nesbitt H. W., Schaufuβ A., Sciani M., Höchst H., Bancroft G. M., and Szargan R. (2003) Monitoring fundamental reactions at NiAsS surfaces by synchrotron radiation X-ray photoelectron spectroscopy: As and S air oxidation by consecutive reaction schemes. *Geochim. Cosmochim. Acta* **67,** 845–858.

Nordstrom D. K. and Alpers C. N. (1999) Geochemistry of Acid Mine Waters. In *The Environmental Geohemistry of Mineral Deposits. Part A: Processes, Techniques and Health Issues, Reviews in Economic Geology* (ed. G. S. Plumlee and M. J. Logsdon), Vol. 6A pp. 133–160, Society of Economic Geologists.

Nordstrom D. K., Alpers C. N., Ptacek C. J., and Blowes D. W. (2000) Negative pH and extremely acidic mine waters from Iron Mountain, California. *Environ. Sci. Technol.* **34,** 254–258.

Norrish K. and Smith D. G. W. (1975) Measurement of oxygen K absorption spectra using an electron microprobe. *X-Ray Spectrometry* **4,** 65–70.

Parks G. A. (1965) The isoelectric points of solid oxides, solid hydroxides, and aqueous hydroxo complex systems. *Chem. Rev.* **65,** 177–198.

Patrito E. M., Olivera P. P., and Sellers H. (1997) On the nature of the SO_4^{2-}/Ag(111) and SO_4^{2-}/Au(111) surface bonding. *Surf. Sci.* **380,** 264–282.

Patterson R. R., Fendorf S., and Fendorf M. (1997) Reduction of Hexavalent Chromium by Amorphous Iron Sulfide. *Environ. Sci. Technol.* **31,** 2039–2044.

Peisert H., Chasse T., Streubel P., Meisel A., and Szargan R. (1994) Relaxation energies in XPS and XAES of solid sulfur compounds. *J. Elec. Spec. Rel. Phenom.* **68,** 321–328.

Peterson M. L., White A. F., Brown G. E., Jr, and Parks G. A. (1997) Surface passivation of magnetite by reaction with aqueous Cr(VI): XAFS and TEM Results. *Environ. Sci. Technol.* **31,** 1573–1576.

Pettenkofer C., Jagermann W., and Bronold M. (1991) Site specific surface interaction of electron donors and acceptors on FeS_2(100) cleavage planes. *Ber. Bunsenges. Phys. Chem.* **95,** 560–565.

Rimstidt J. D. and Vaughan D. J. (2003) Pyrite oxidation: a state-of-the-art assessment of the reaction mechanism. *Geochim. Cosmochim. Acta* **67,** 873–880.

Rosso K. M., Becker U., and Hochella M. F., Jr.. (1999a) Atomically resolved electronic structure of pyrite {100} surfaces: An experimental and theoretical investigation with implications for reactivity. *Am. Mineral.* **84,** 1535–1548.

Rosso K. M., Becker U., and Hochella M. F., Jr.. (1999b) The interaction of pyrite {100} surfaces with O_2 and H_2O: Fundamental oxidation mechanisms. *Am. Mineral.* **84,** 1549–1561.

Sasaki K., Tsunekawa M., Ohtsuka T., and Konno H. (1995) Confirmation of a sulfur-rich layer on pyrite after oxidative dissolution by Fe(III) ions around pH 2. *Geochim. Cosmochim. Acta* **59,** 3155–3158.

Sasaki K., Tsunekawa M., Ohtsuka T., and Konno H. (1997) Reply to the Comment by G. W. Luther III on "Confirmation of a sulfur-rich layer on pyrite after oxidative dissolution by Fe(III) ions around pH 2." *Geochim. Cosmochim. Acta* **61,** 3273–3274.

Schaufuβ A. G., Nesbitt H. W., Kartio I., Laajalehto K., Bancroft G. M., and Szargan R. (1998a) Incipient oxidation of fractured pyrite surfaces in air. *J. Elec. Spec. Rel. Phenom.* **96,** 69–82.

Schaufuβ A. G., Nesbitt H. W., Kartio I., Laajalehto K., Bancroft G. M., and Szargan R. (1998b) Reactivity of surface chemical states on fractured pyrite. *Surf. Sci.* **411,** 321–328.

Schaufuβ A. G., Nesbitt H. W., Scaini M. J., Höchst H., Bancroft G. M., and Szargan R. (2000) Reactivity of surface chemical sites on fractured arsenopyrite (FeAsS) towards oxygen. *Am. Mineral.* **85,** 1754–1766.

Schedel-Niedrig T., Neisius T., Simmons C. T., and Köhler K. (1996) X-ray absorption spectroscopy of small chromium oxide particles (Cr_2O_3, CrO_2) supported on titanium dioxide. *Langmuir* **12,** 6377–6381.

Sherman D. M. (1985a) The electronic structures of Fe^{3+} coordination sites in iron oxides: Applications to spectra, bonding, and magnetism. *Phys. Chem. Miner.* **12,** 161–175.

Sherman D. M. (1985b) SCF-Xα-SW study of Fe-O and Fe-OH chemical bonds: Application to the Mossbauer spectra and magneto chemistry of hydroxyl-bearing iron oxides and silicates. *Phys. Chem. Miner.* **12,** 311–314.

Sherman D. M. and Waite T. D. (1985) Electronic spectra of Fe^{3+} oxides and oxide hydroxides in the near IR to near UV. *Am. Mineral.* **70,** 1262–1269.

Simón M., Ortiz I., García I., Fernández E., Fernández J., Dorronsoro C., and Aguilar J. (1999) Pollution of soils by the toxic spill of a pyrite mine (Aznalcollar, Spain). *Sci. Total Envir.* **242,** 105–115.

Singer P. C. and Stumm W. (1970) Acidic mine drainage: rate-determining step. *Science* **167,** 1121–1123.

Smart R. S. C., Skinner W. M., and Gerson A. R. (1999) XPS of sulfide mineral surfaces: metal-deficient, polysulfides, defects and elemental sulphur. *Surf. Interface Anal.* **28,** 101–105.

Stöhr J. (1988) *NEXAFS Spectroscopy.* Springer-Verlag.

Thole B. T. and Van der Laan G. (1988) Branching ratio in x-ray absorption spectroscopy. *Phys. Rev. B.* **31,** 3158–3171.

Todd E. C. and Sherman D. M. (2003) Surface oxidation of chalcocite (Cu_2S) under aqueous (pH = 2–11) and ambient atmospheric conditions: Mineralogy from Cu *L*- and O *K*-edge X-ray absorption spectroscopy. *Am. Mineral.* **88,** 1652–1656.

Todd E. C., Sherman D. M., and Purton J. A. (2003a) Surface oxidation of chalcopyrite ($CuFeS_2$) under ambient atmospheric and aqueous (pH 2–10) conditions: Cu, Fe *L*- and O *K*-edge X-ray spectroscopy. *Geochim. Cosmochim. Acta* **67,** 2137–2146.

Todd E. C., Sherman D. M., and Purton J. A. (2003b) Surface oxidation of pyrite under ambient atmospheric and aqueous (pH = 2 to 10) conditions: electronic structure and mineralogy from X-ray absorption spectroscopy. *Geochim. Cosmochim. Acta* **67,** 881–893.

Uhlig I., Szargan R., Nesbitt H. W., and Laajalehto K. (2001) Surface states and reactivity of pyrite and marcasite. *App. Surf. Sci.* **179,** 223–230.

van Aken P. A., Liebscher B., and Styrsa V. J. (1998) Core level electron energy-loss spectra of minerals: pre-edge fine structures at the oxygen K-edge Comment on "Water in minerals detectable by electron energy-loss spectroscopy EELS" by R. Wirth. *Phys. Chem. Miner.* **25,** 494–498.

Waychunas G. A. (1991) Crystal Chemistry of the Oxides and Hydroxides. *Rev. Mineral.* **25,** 11–68.

White A. F. and Peterson M. L. (1996) Reduction of aqueous transition metal species on the surfaces of Fe(II)-containing oxides. *Geochim. Cosmochim. Acta* **60,** 3799–3814.

Wirth R. (1997) Water in minerals detectable by electron energy-loss spectroscopy. *Phys. Chem. Miner.* **24,** 561–568.

Wirth R. (1998) Water in minerals detectable by electron energy-loss spectroscopy EELS: Reply to "Core level electron energy-loss spectra of minerals: pre-edge fine structures at the oxygen K-edge" by P.A. van Aken et al. *Phys. Chem. Miner.* **25,** 499–500.

Wu Z. Y., Gota S., Jollet F., Pollack M., Gautier-Soyer M., and Natoli C. R. (1997) Characterization of iron oxides by x-ray absorption at the oxygen *K* edge using a full multiple scattering approach. *Phys. Rev. B.* **55,** 2570–2577.

Zouboulis A. I., Kydros K. A., and Mathis K. A. (1995) Removal of hexavalent chromium anions from solutions by pyrite fines. *Wat. Res.* **29,** 1755–1760.